

# A Numerical Method for Microstructure Generation of a Binary Aluminum Alloy and Study of Its Mechanical Properties Using the Finite Element Method

HAMID SHARIFI and DANIEL LAROUCHE

A numerical method for the generation of the microstructure of a binary aluminum copper alloy is presented. This method is based on the repeated addition of some basic grain shapes into a representative volume element. Depending of the orientation of adjacent grains, different type of grain boundaries can be formed. The primary and secondary phases are distinguishable in our model and have distinct properties, reflecting the heterogeneous nature of the microstructure. The digital microstructure was then transformed into a finite element model. Using the finite element software ABAQUS, the stress distribution inside our heterogeneous material model has been studied and its mechanical properties have been found. That also makes possible to study and to visualize the cracks generated during the loading of the material where the local stress was sufficiently high. As a result of these analyses, the elastic modulus of such a heterogeneous domain and the effect of crack formation on ductility were evaluated.

DOI: 10.1007/s11661-014-2446-3

© The Minerals, Metals & Materials Society and ASM International 2014

## I. INTRODUCTION

THE classical stress analysis approaches based on continuum mechanics give the modeling tools for computation of stress field inside a homogeneous material. This type of modeling is not able to give the localized stress concentration inside a real material because it cannot take into account its microstructure. As an example, a fracture apparition and nucleation cannot be explained adequately based on continuum mechanics theories.

A lot of engineering materials have polycrystalline and multiphase structures. The overall mechanical properties of these materials depend on the properties of these crystals (grains). An old fundamental principle in the analysis of materials is the structure-properties relationship which states that there is an undeniable relation between the structure of a material and its properties.<sup>[1]</sup> The structure can be interpreted at the atomic, the crystal lattice, or at the grain microstructure level. An important scale which affects the mechanical properties and stress distribution inside a material is the grain microstructure of the material. An individual crystal could be anisotropic in both elastic and plastic behaviors, but if a volume of material contains a large numbers of grains with random crystal lattice orientations, it could present isotropic characteristics. Even if

the overall mechanical property of a material is considered as isotropic, the stress distribution inside a volume of the material depends on its grain microstructure. As a result, the geometrical grain structures of a material at the microstructural scale can help us to understand stress field variations inside a material.

Several authors have worked on the development of microstructure models for the simulation of recrystallization and grain growth problems. These models can be divided into two groups.<sup>[2]</sup> The geometrical and topological model of the first group is based on combining the elementary geometry of nucleation, grain growth, and impingement.<sup>[3-6]</sup> These models are mostly constructed by employing the Voronoi's structure where the initial nucleation points are seeds in the Voronoi's diagram. The second group, which is called component methods, is an extension of the first group to include several components like for example the grain orientations.<sup>[7,8]</sup> Nucleation and growth conditions are defined for each component. Different texture components grow independently and the final microstructure is formed when growing grains impinged and prevent their further growth. The nuclei can be distributed initially or they can be added continuously. The component method can be used for a three-dimensional (3D) simulation too. An interesting method for modeling microstructure evolution processes is the phase-field method. This method defines a microstructure as a whole using some field variables which are functions of space.<sup>[9]</sup> Microstructure model can also be captured directly from microstructure photography for creating a digital microstructure model, here image processing techniques are used to produce such granular models.<sup>[10,11]</sup>

When an acceptable microstructure geometric with distinguishable solid phases has been produced, the overall mechanical properties of the material can be

---

HAMID SHARIFI, Research Associate, is with the Department of Mechanical Engineering, Aluminum Research Center – REGAL, Laval University, 1065, Ave de la Médecine, Quebec, QC G1V 0A6, Canada. Contact e-mail: hamid.sharifi@gmn.ulaval.ca DANIEL LAROUCHE, Professor, is with the Department of Mining, Metallurgy and Materials Engineering, Aluminum Research Center – REGAL, Laval University.

Manuscript submitted January 24, 2014.

Article published online September 16, 2014

found. There exist different approaches from different scales that can be used to calculate such properties; some of them are reviewed by Ortiz and Phillips.<sup>[12]</sup> Atomistic simulation is a powerful method to evaluate the mechanical properties of materials. However, it has serious difficulties, among them the limitation to work with small sizes and application of boundary conditions. Higher-level methods used by several researchers are based on polycrystal plasticity.<sup>[13–16]</sup> Here finite element formulations are used to describe the plasticity in the various grains. Some two dimensional models were presented by Becker and McHugh *et al.*<sup>[15,16]</sup> Beaudoin *et al.* presented a three-dimensional finite element model for crystal plasticity with a viscoplastic constitutive formulation. The polycrystal was constructed by three-dimensional cuboid grains which formed a 2 by 2 by 2 array. Each grain can have different orientation, constitutive response, and is discretized to finer finite elements. Using such an approach, localized orientation gradients in face-centered polycrystals and the evolution of nonuniform deformation zones within individual crystals were simulated.

In this paper, a new method for producing discretized microstructure of alloys is presented. The grain growth formulations are not used in this approach. We only focused on the generation of a realistic final microstructure, avoiding the complicated procedures normally required by precipitation and growth of solid phases. As this will be shown in this paper, the generated microstructures mimic satisfactorily the 2D features of real microstructures and can be tailored to different grain sizes and morphologies (globular dendritic, fine, ultra-fine) using a proper set of basic grain shapes. The generated microstructure is transformed automatically into a finite element mesh. Using the ABAQUS software package, we have investigated the mechanical properties of an as-cast material, namely the binary Al-4.6 pct Cu alloy.

## II. GRAIN GENERATIONS

Consider a tensile test of a solid material using a specimen with a uniform and thin thickness, as shown in Figure 1.

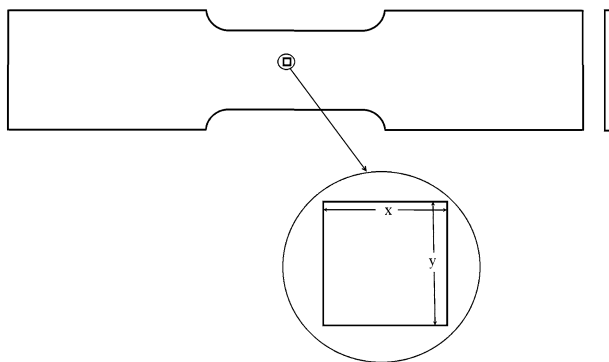


Fig. 1—A tensile test specimen and a piece of such a specimen.

As the thickness of the specimen is considerably smaller than its other dimensions, it is almost a plane stress problem. Now, consider a piece of such a test specimen that contains all the solid phases which have been formed during the solidification or after the heat treating process. For example, for an as-cast material this piece of material must be big enough to contain several solid grains and secondary phases, so it is able to demonstrate the heterogeneous characteristic of the solid material satisfactory. For the simplicity, a rectangular domain having  $x, y$  dimensions can be used.

Our method is based on the creation of the grains inside this rectangular piece of material, which from now on will be called the representative volume element (RVE). As an example, we will consider the binary aluminum alloy having 4.6 pct copper in the as-cast condition. In the Aluminum rich part of the aluminum-copper phase diagram, shown in Figure 2, one can see that the face-centered-cubic (FCC) phase  $\alpha$  and the intermetallic phase  $\theta$  ( $\text{Al}_2\text{Cu}$ ) can coexist in this alloy. The volume fraction and morphology of the secondary phase in the as-cast specimens will depend on the cooling condition because of the solute redistribution phenomena.<sup>[17]</sup> If solidification occurs close to equilibrium, the  $\theta$  phase precipitates in the matrix phase  $\alpha$  *via* a solid state transformation. However, if the cooling rate is sufficiently fast, like those encountered in regular casting operations, the  $\theta$  phase precipitates from the liquid phase *via* a eutectic reaction. This is the general situation of as-cast specimens and one of the difficulties is to estimate the volume percentage of each phase. Nowadays, the volume fractions can be calculated with precision with a solidification model using the Scheil–Gulliver assumption or assuming back diffusion in the matrix phase.<sup>[18]</sup> Alternatively, the volume fractions can be determined by image analysis.<sup>[19]</sup>

### A. Basic Grain Shapes

To create grains, some basic grain shapes must be chosen. For the binary aluminum 4.6 pct copper alloy, which has in as-cast condition a certain amount of  $\theta$

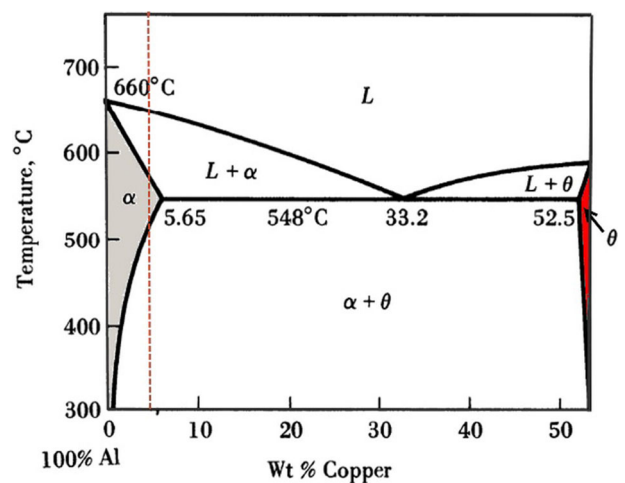


Fig. 2—Part of Al-Cu phase diagram. Adapted from Ref. [31].

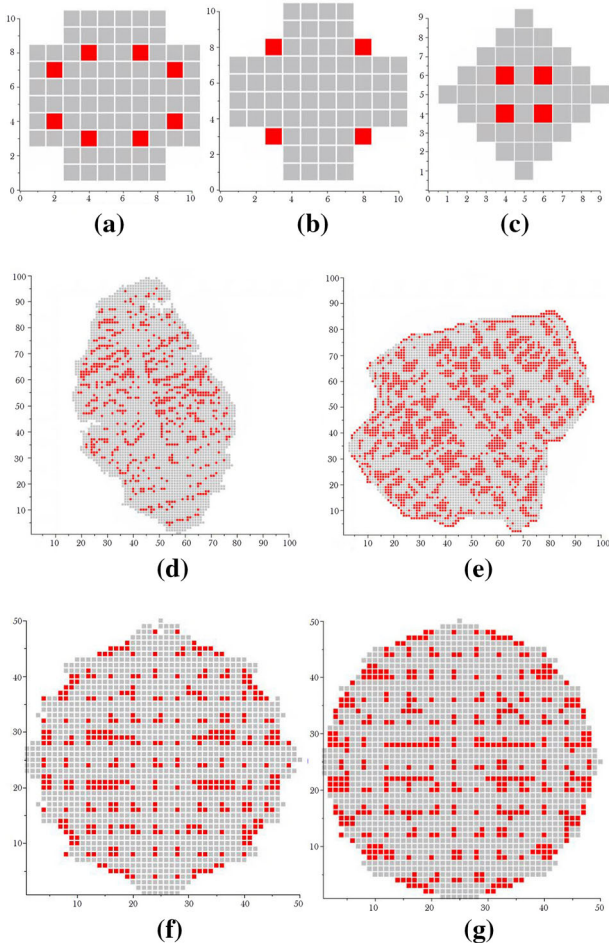


Fig. 3—Some basic grain shapes. Gray squares are  $\alpha$  phase elements and red squares are  $\theta$  phase elements (Color figure online).

phase, one can try some of the basic grain shapes shown in Figure 3. The gray squares in these figures represent the  $\alpha$  phase elements while the red ones represent the  $\theta$  phase elements.

The basic grains shown in Figures 3(d) and (e) are constructed in an array of 100 by 100 elements and better reproduce the complexity of real grain geometries. The 100 by 100 elements array can therefore be used for a more realistic representation of grains but at a higher computational cost. These shapes give realistic grain microstructures because they were captured from a real micrograph. The quality of the final microstructure depends on the resolution of the basic grain shapes. The basic grains shown in Figures 3(f) and (g) have intermediate resolution since they are constructed in a 50 by 50 elements array. Taking into account the volume of computer memory needed and the speed of calculation, we mostly used 50 by 50 basic grain models for the grain generation and the finite element analysis.

### B. General Procedure

The general procedure is as follows: take a RVE completely fill with the  $\theta$  phase, a basic grain shape is randomly selected from a predefined basic grain shapes

library, its orientation and its size are chosen randomly, and then it is placed in a random position inside the RVE. Figures 4(a) through (f) present some shapes of the RVE in such a procedure. In these figures, the white regions are  $\alpha$  phase regions. As it can be seen from Figure 4, some basic shapes will intersect each other inside the RVE, so some intersection rules are needed, the latter depending on the grain orientation. The basic grains insertion is continued until one obtains a given volume fraction of  $\alpha$  and  $\theta$  phases, the latter having been previously determined from the phase diagram or from experimental measurements.

Before placing a basic grain in the RVE, to have a random orientation of the grain for the generation of an equiaxed microstructure, a basic grain must be rotated by a random angle. The basic grain shapes are composed from small upright rectangles, as a result each element can be identified from two integer numbers which present its  $x$  and  $y$  coordinates. For example, for a grain presented in a 10 by 10 array each element can be addressed from two integers from 1 to 10. To have a simple finite elements mesh generation procedure, it is preferable to preserve the composition of the grains from small upright rectangles and the integer addressability of each rectangle after a rotation. So, for each rectangle, the position of its geometrical center after the rotation is determined, then upright rectangles are placed in every integer position close to this coordinates.

To have a continuous grain boundary, sometime it is necessary to place several rectangles in place of one. The selection of the nearby rectangles for a given grain boundary line is somehow similar to Bresenham's line algorithm used in line drawing in computer graphics.<sup>[20]</sup> Figures 5(a) through (c) present several rotations of a 10 by 10 rectangle. Figures 5(d) and (e) present a 50 by 50 array grain before and after 45 deg rotation. As it can be seen the rotated grains are not exactly the same as the original one and sometime even  $\theta$  phase may be replaced by solid phase or vice versa. This does not cause any problem as the objective is the generation of random grains so these types of deviations even generate a better result.

### C. Connection Criteria

After the creation of basic grain shapes, they must be projected into the RVE to obtain a granular structure. In the projection procedure, the size, the position, and the orientation of each grain inside the RVE are chosen randomly. When a new grain occupy an area already covered by a previous grain, a connection criterion is needed to decide whether these grains must be connected together or a new grain, with a  $\theta$  phase joining band separator, must be inserted.

Hasson and Goux<sup>[21]</sup> considered the grain boundary energy for an aluminum alloy. They presented the grain energy ( $\gamma_{gb}$ ) as a function of the misorientation angle of the grains ( $\Delta\theta$ ). A simple approximation of this function, which is given by Mathier *et al.*,<sup>[22]</sup> is presented in Figure 6.



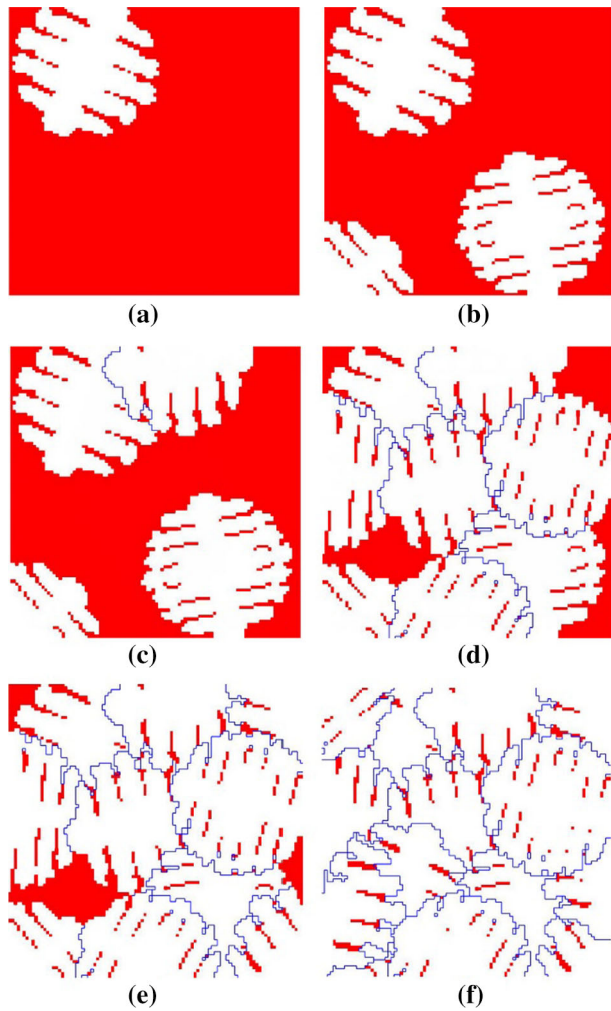


Fig. 4—Insertion of basic grains inside a RVE.

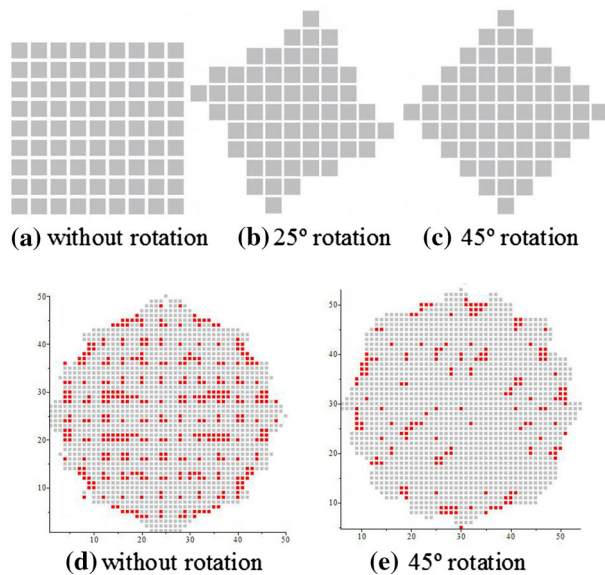


Fig. 5—(a) Through (c) rotation of a 10 by 10 rectangular shape, (d) and (e) rotation of a 50 by 50 basic grain by 45 deg.

Rappaz *et al.*<sup>[23]</sup> considered merging and coalescence of two flat solid–liquid interfaces of unit area. They stated that the coalescence can be seen as the disappearance of two solid–liquid boundaries, each with energy  $\gamma_{s/l}$ , and the formation of a solid–solid grain boundary with energy  $\gamma_{gb}$ . Consider the case where  $\gamma_{gb} < 2\gamma_{s/l}$ , here the free energy will be decreased if the solid–solid junction is formed. So it is an attractive situation.

Looking at Figure 6, it can be seen that such a situation will occur for a low-orientation difference between two adjacent grains, namely if  $0 \text{ deg} \leq \Delta\theta \leq 11 \text{ deg}$  and  $79 \text{ deg} \leq \Delta\theta \leq 90 \text{ deg}$ . If  $\gamma_{gb} = 2\gamma_{s/l}$  then the free energy stays the same whether or not the solid–solid junction is formed. This refers to the neutral case. On the other hand, if  $\gamma_{gb} > 2\gamma_{s/l}$ , then the free energy will be increased if the solid–solid junction is formed. So it is a repulsive situation. Considering Figure 6, one concludes that such a situation will occur for high-orientation differences between two adjacent grains.

As a result, if a part of the position of the inserted grain is already occupied with the previous grain in the domain, the decision about the type of junction between the inserted grain and the old one will depend on the orientation difference between these two grains. If it is an attractive case, the grains must be connected and a single grain is formed. If it is a repulsive case, the old grain must be cut and a new grain is inserted in its position. Between the cut and the new grain, a  $\theta$  phase joining band (channel) must be inserted to separate these grains. The existence of this phase at the intergranular position is to mimic the late solidification of the liquid phase, rich in copper, existing between the grains. Here, it is assumed that the liquid is forming a divorced eutectic microconstituent where the  $\theta$  phase remains as a continuous phase at the boundary.

To compare the generated microstructure with a real binary microstructure, the B206 aluminum alloy having the chemical composition shown in Table I was used from the works described in Reference 24.

Although commercial B206 has small amounts of several additional alloying elements beside copper, like manganese, magnesium, silicon, iron, zinc, titanium, and nickel, which have some role in its mechanical

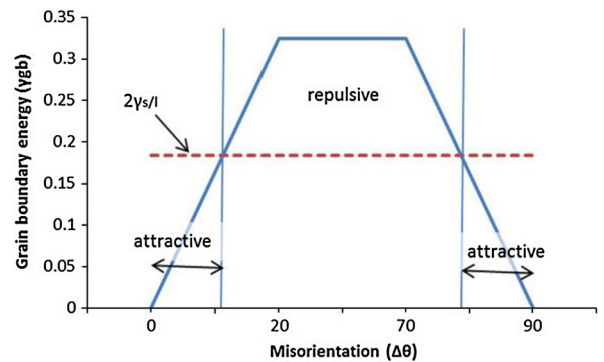


Fig. 6—Grain boundary energy versus misorientation ( $\Delta\theta$ ) in an aluminum alloy.

**Table I. B206 Alloy Composition, Weight Percent**

Cu	4.60
Fe	0.06
Si	0.10 (out of specification)
Mn	0.40
Mg	0.25
Ti	<0.01
Zn	0.00
Ni	<0.01
Fe/Si	0.60
Al	balance

properties, the main characteristics of the alloy depends on its copper content. For simplicity, we will then consider it as a binary aluminum alloy.

Figure 7(a) shows the microstructure of an as-cast B206 specimen having approximately a volume fraction 95.6 pct of  $\alpha$  phase and an average grain size of 550  $\mu\text{m}$ . Figure 7(b), shows the grains digitally created for the same volume fraction of  $\alpha$  phase in a 4 mm by 4 mm square RVE. The basic grain shapes a, b and c of Figure 3 were used with a resolution of 50  $\mu\text{m}$  by 50  $\mu\text{m}$  (size of the square elements composing the grain shapes). The blue lines are the joining  $\theta$  phase channels

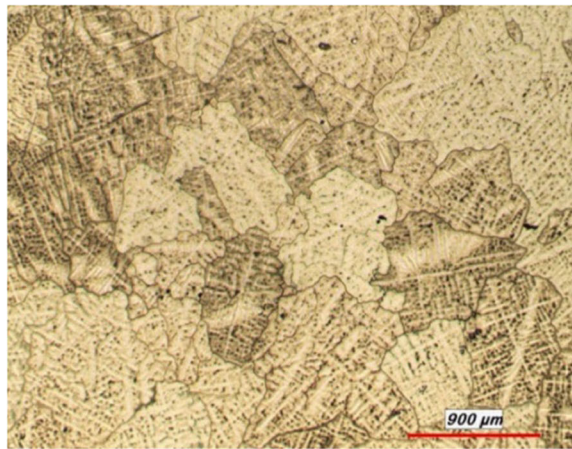
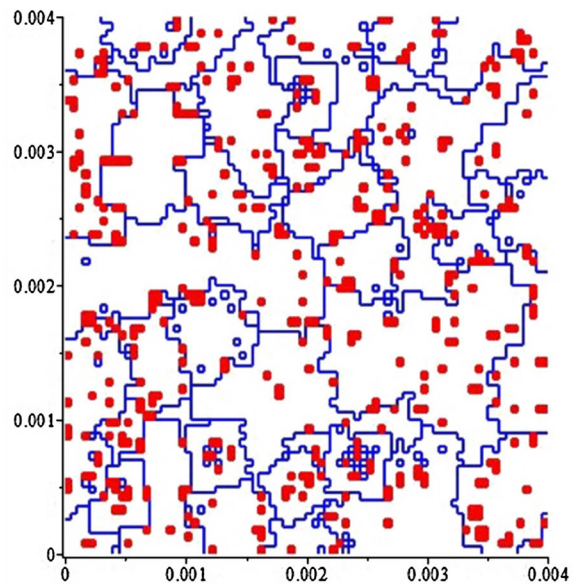
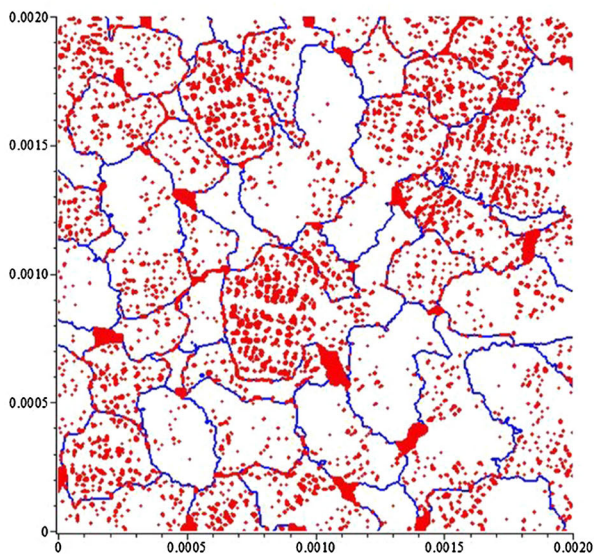
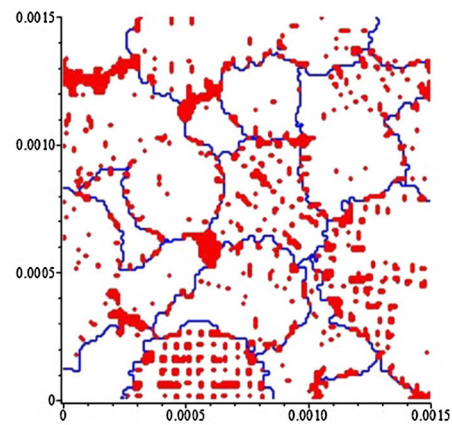
**(a)****(b)****(c)****(d)**

Fig. 7—(a) A photograph of the micro-structure of as-cast B206. This picture was taken from specimens prepared during the works described in Ref. [24]. (b) Generated microstructure using basic grain shapes a, b, and c of Fig. 3. (c) Generated microstructure using the basic grain shapes d and e. (d) Generated microstructure using the basic grain shapes f and g.



generated by the grain connection procedure. The red squares are the  $\theta$  phase elements that: 1—came with the basic grains and 2—remained between the grains once the insertion procedure finished. The comparison of this figure with Figure 7(a) show that, even with simple basic grain shapes of low resolution, the microstructure of this alloy is simulated satisfactorily.

Figure 7(c) presents the generated grains for the same alloy in a 2 mm by 2 mm square RVE with elements of 5  $\mu\text{m}$  by 5  $\mu\text{m}$  in size using the basic grain shapes d and e of Figure 3. As it can be seen the generated microstructure is very similar to what can be seen in a real micrograph. This illustrates the potentiality of our grain generation method to create complicated microstructures in a simple way. For an intermediate grain resolution, Figure 7(d) shows the generated grains for a 1.5 mm by 1.5 mm square RVE with the element of size 10  $\mu\text{m}$  by 10  $\mu\text{m}$  using the basic grain shapes f and g of Figure 3.

#### D. Thickness of the $\theta$ Phase Channels

Each generated grain structure is constructed for a given  $\alpha$  to  $\alpha + \theta$  fraction determined according to the solidification path. One can divide the  $\theta$  fraction in two parts; the first part contains the  $\theta$  phase between the grains wetting at least two grains and the  $\theta$  phase inside the grain, which is already included in the basic grain shape. This subset of  $\theta$  phase will be designated “pockets”. The second part contains the  $\theta$  phases which exist in the form of channels between the grains made from a repulsive contact between the grains. This subset of  $\theta$  phase will be designated “channel”. The volume fraction of these two subsets of  $\theta$  phase can be written as follows:

$$F_{\theta} = F_{\theta P} + F_{\theta C}. \quad [1]$$

Here,  $F_{\theta}$  is the global fraction of  $\theta$  phase,  $F_{\theta P}$  is the fraction of  $\theta$  phase pockets, and  $F_{\theta C}$  is the fraction of  $\theta$  phase channels. These values must be evaluated before starting the grain generation procedure. For instance, it is known that the volume fraction of channels depends on the cooling rate because of the combined effects of microsegregation and back-diffusion phenomena. So, an estimation of channel thicknesses is required to generate a suitable microstructure. A more comprehensive treatment of this topic can be found in Reference 25.

At the beginning, the RVE is composed of  $N$  by  $N$  elements. A fraction  $F_{\theta P}$  of these elements will be  $\theta$  phase at the end of the projection procedure. It is important to mention that channel elements will be added after this step. Since all elements have the same initial size at the projection procedure, one can write at this stage:

$$F_{\theta P} = \frac{\text{Number of } \theta \text{ elements}}{\text{Total number of elements in the control volume}}. \quad [2]$$

The volume of  $\theta$  phase inside the channels ( $V_{\theta C}$ ), is given by.

$$V_{\theta C} = F_{\theta C} \cdot V_{\text{RVE}}, \quad [3]$$

where  $V_{\text{RVE}}$  is the volume of the RVE. Let  $v_i$  be the volume of a channel segment  $i$  separating two adjacent elements, each belonging to different grains. The volume of channels must be equal to the sum of all these segments so one can write:

$$V_{\theta C} = \sum_i v_i. \quad [4]$$

Channel segments may have different thicknesses ( $\delta_i$ ). If  $l_{\text{elem}}$  is the length of the channel segment separating two adjacent elements, then we have:

$$v_i = \delta_i \cdot l_{\text{elem}}. \quad [5]$$

For each pair of adjacent grains, a random channel thickness  $\delta_i$  is assumed and is given as:

$$\delta_i = k \cdot r_i, \quad [6]$$

where  $r_i$  is a random real number between 0.0 and 1.0 and  $k$  is a scaling factor, which must be determined to satisfy Eq. [3].

As a result, one can write:

$$V_{\theta C} = \sum_i v_i = l_{\text{elem}} \cdot \sum_i \delta_i = l_{\text{elem}} \cdot k \cdot \sum_i r_i. \quad [7]$$

Now, this equation can be solved for  $k$ .

$$k = \frac{V_{\theta C}}{l_{\text{elem}}} \cdot \sum_i r_i. \quad [8]$$

### III. FINITE ELEMENTS MESH GENERATION

Creation of  $\alpha$  phase finite elements are straightforward since each  $\alpha$  element of the discrete domain can be presented as an  $\alpha$  phase finite element. This is also true for the  $\theta$  pocket zones as each  $\theta$  element of the discrete domain can be converted to a  $\theta$  phase finite element. The sole difficulty is the presentation of the  $\theta$  phase channels. The  $\theta$  phase channels are between two solid elements. The sizes of these channels, using calculations of the pervious section, are already known. To create them, as shown in Figures 8(a) and (b), parts of the adjacent elements in both side of the channel are taken and a  $\theta$  phase finite element is created from these parts. To have a uniform finite elements mesh, half of the  $\theta$  phase channel thickness is taken from each adjacent  $\alpha$  elements. Notice that these elements belong to different grains so they can have different orientations. Figure 8(c) shows an example of the finite element generation in a portion of a generated microstructure.

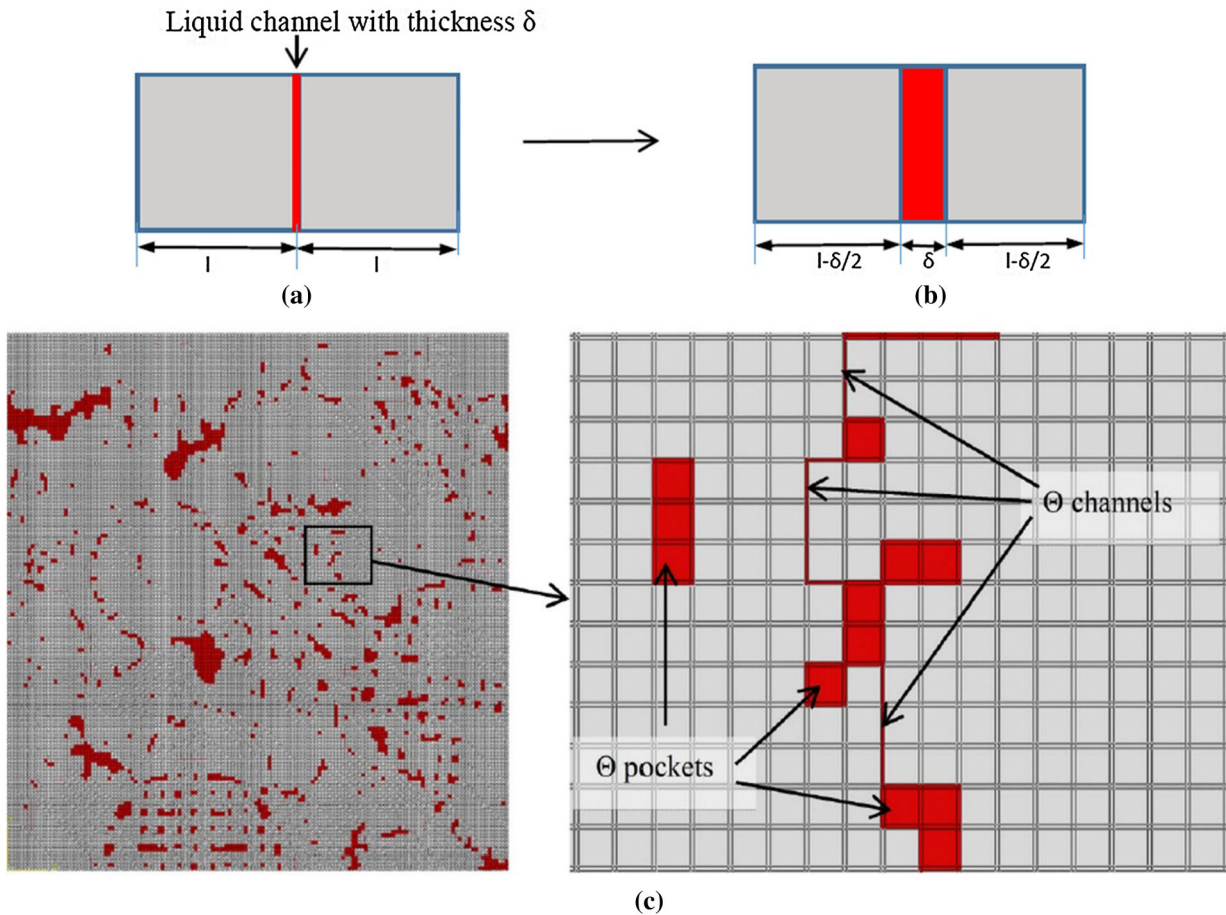


Fig. 8—(a), (b) Creation of a  $\theta$  phase channel finite element from two adjacent solid elements. (c) Finite element mesh.

#### IV. NUMERICAL RESULTS

Using our grain generation procedure, different grain structures have been created and converted into finite element meshes. Each mesh was thereafter introduced in the finite element software package ABAQUS. The Al-4.6 pctCu was considered to have 4.4 vol pct of  $\theta$  phase, among which, 2.5 vol pct was presented in the channels generated by the connection procedure. The thickness of each channel was chosen randomly under the constraint that the overall targeted vol pct of  $\theta$  phase was met. The scaling of the grains was adjusted in order that the average grain size obtained was equal to  $550 \mu\text{m}$ . Different loading and boundary conditions were applied. As  $\alpha$  phase can have plastic deformation before failure, but  $\theta$  phase is brittle and it does not have a plastic deformation,<sup>[26]</sup> in these analyses, the  $\alpha$  phase elements were considered as an elastoplastic material and the  $\theta$  phase as an elastic material until its fracture point.

##### A. Mechanical Properties of an As-Cast Material

Figure 9 presents the finite element mesh and the boundary conditions applied on the 1.5 mm by 1.5 mm RVE presented in Figure 7(d). The elements of the first

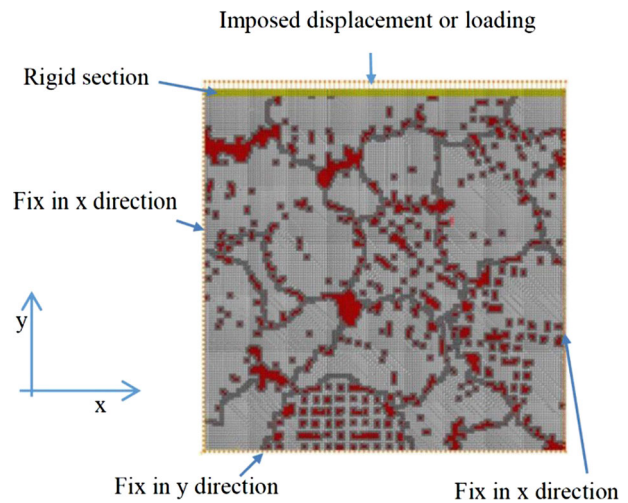


Fig. 9—Finite element model of a 1.5 mm by 1.5 mm RVE.

5 rows from the top are considered rigid to be able to apply the tension load to the top of the domain. The bottom nodes are fixed in the  $y$  direction and the side nodes are fixed in the  $x$  direction. The elastoplastic material parameters implemented in ABAQUS are presented in Table II.

**Table II. Mechanical Properties of the Phases**

Phase	Young's Modulus (GPa)	Poisson's Ratio	Yield Strength (MPa)	Ultimate Strength (MPa)	Elongation (pct)	Copper (pct)	Other Elements (pct)
$\alpha$	70	0.34	165	295	24	2.6	0.35
$\alpha$ near $\theta$	73	0.34	395	475	10	6.3	0.36
$\theta$	110	0.34	1100				

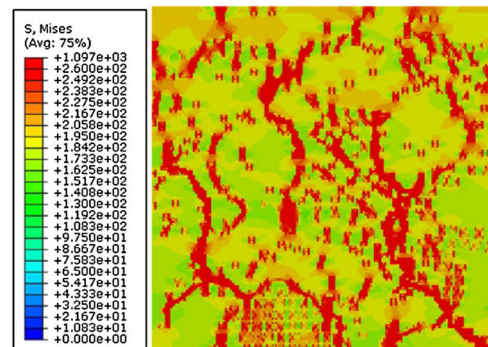
For an as-cast Al-Cu alloy, it is well known that the copper concentration varies from the center of a dendrite to its boundary because of the microsegregation phenomenon.<sup>[27]</sup> For an Al-4.6 pct Cu, the Cu concentration can vary from 2 wt pct in the center of the dendrite to 5 wt pct near the edge, so the material properties are expected to be not uniform in the  $\alpha$  phase. It was therefore decided to give the material properties of an aluminum alloy having a Cu content close to 5 pct and being in the state of fully homogenized for the elements located at the boundary of the  $\alpha$  phase. The properties associated to the  $\alpha$  phase elements near  $\theta$  (here  $\alpha$  elements in contact with  $\theta$  element) were taken from B2219-T87 (Al-6.3wt pctCu) alloy. The others not located on the periphery were given properties of the B2117-T4 (Al-2.6 wt pct Cu). The properties of the above mentioned alloys were taken from Reference 28. A variable displacement boundary condition was applied at the top of RVE. The imposed displacement started from zero and increased linearly until it reaches its maximum value before the breakdown of the RVE, occurring here after a displacement of 0.037 mm. Using the *static general* step of the finite element analysis of the ABAQUS software, two dimensional plane stress problems have been solved.

Figure 10(a) presents the Von-Mises stresses obtained at an axial deformation of  $\epsilon = 0.022$ . If one compares Figure 10(a) with Figure 7(d), one can see that the grain boundary zones are transferring a considerable amount of loading from top to bottom of the RVE. Figure 10(b) presents the distribution of the Von-Mises stresses at the same imposed strain for the discretized microstructure presented in Figure 7(c). The latter have a resolution of 5  $\mu\text{m}$  instead of 10  $\mu\text{m}$  in Figure 10(a).

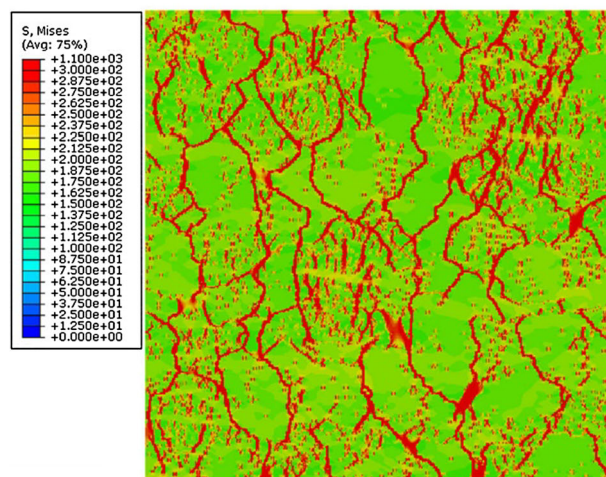
If one calculates the average stress as the sum of nodal reaction forces at the bottom of the RVE over the cross section area and the average strain as the displacement of the top nodes over the height of the RVE, a stress-strain curve can be drawn. Those presented in Figure 11 were obtained with the discretized microstructures presented in Figures 7(c) and (d).

Although the microstructures have obvious differences, they produce similar stress strain curves. The elastic moduli, yield stresses and elongations are almost the same but we observe a little difference in ultimate stresses which likely indicates that grain shapes have a measurable influence on the rupture mechanism.

To compute the Young's modulus of the RVE we consider the whole RVE as a plane stress element. For an elastic plane stress element the relation between stresses and strains are:



(a)  $\epsilon = 0.022$ , for a 1.5 by 1.5mm RVE



(b)  $\epsilon = 0.022$ , for a 2 by 2mm RVE

Fig. 10—(a) Von-mises stresses inside the RVE of the microstructure of Fig. 6(d), (b) Von-mises stresses inside the RVE of the microstructure of Fig. 6(c).

$$\begin{bmatrix} \sigma_{xx} \\ \sigma_{yy} \\ \tau_{xy} \end{bmatrix} = \frac{E}{1-\nu^2} \begin{bmatrix} 1 & \nu & 0 \\ \nu & 1 & 0 \\ 0 & 0 & (1-\nu)/2 \end{bmatrix} \begin{bmatrix} \epsilon_{xx} \\ \epsilon_{yy} \\ \gamma_{xy} \end{bmatrix}, \quad [9]$$

where  $E$  is the Young's modulus and  $\nu$  is the Poisson's ratio. Using our boundary conditions presented in Figure 9, it can be understood that  $\epsilon_{xx} = 0$  and  $\gamma_{xy} = 0$ .

So, we have:

$$E = \frac{\sigma_{yy}}{\epsilon_{yy}} (1 - \nu^2). \quad [10]$$

After the finite element execution the  $\epsilon_{yy}$  at the top of the RVE is known and the  $\sigma_{yy}$  can be evaluated as the



sum of the reaction forces at the bottom of the RVE divide by the cross section area, so the Young's modulus can be calculated simply.

The comparison of our simulation results with an as-cast B206 alloy (aluminum 4.6 pct copper) measurements is presented in Table III. As it can be seen from this table, our results match very well with those of the measured mechanical properties of as-cast B206.

It is worth noting that some mechanical properties of B206 alloy have been reported in Reference 29 but we have limited our work to the B206 specimens is as-cast condition for which we had experimental data and actual pictures of the microstructure.

Using the microstructure model, the crack appearance and propagation inside the RVE can be simulated. Here, the element elimination option of ABAQUS software package has been used. The damage criterion model for the ductile material of ABAQUS initiates the damage when the equivalent plastic strain reaches a critical value which is a function of stress triaxiality and strain rate,<sup>[30]</sup> *i.e.*,  $\bar{\epsilon}_D^{pl}(\eta, \dot{\bar{\epsilon}}^{pl})$ . Here,  $\eta = -\frac{p}{q}$  is the stress triaxiality,  $p$  is the pressure stress,  $q$  is the Mises equivalent stress, and  $\bar{\epsilon}^{pl}$  is the equivalent plastic strain rate. The damage initiation will occurred once:

$$\int \frac{d\bar{\epsilon}^{pl}}{\bar{\epsilon}_D^{pl}} = 1.$$

When the equivalent plastic strain becomes larger than  $\bar{\epsilon}_D^{pl}$ , the element becomes less effective using a certain damage evaluation rule and finally it is eliminated. In our analysis, tensile test data of each phase given in Table II is used and when the equivalent plastic strain inside an element becomes larger than the fracture strain, the failed element is eliminated rapidly.

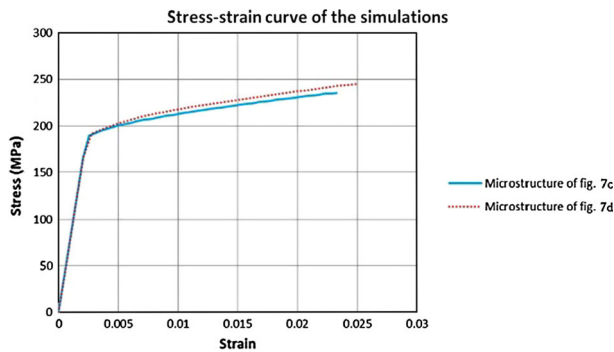


Fig. 11—Overall stress–strain curves obtained with the discretized microstructures presented in Fig. 7(c) (blue line) and Fig. 7(d) (red dotted line) (Color figure online).

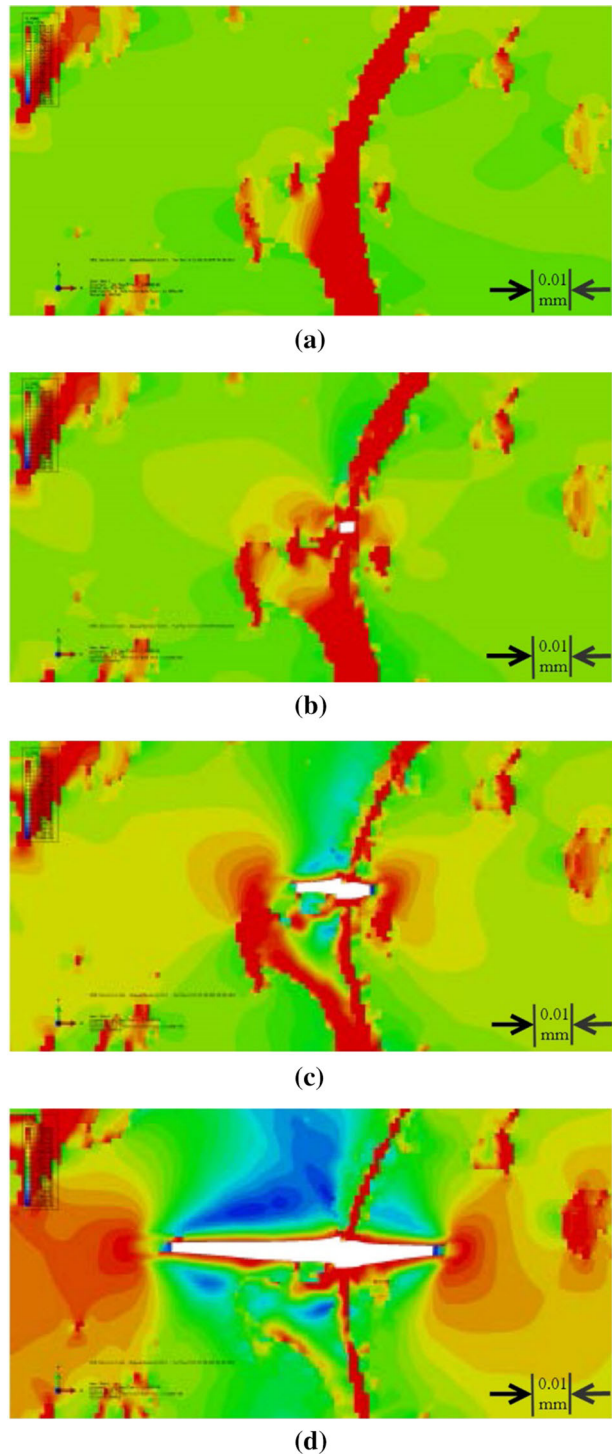


Fig. 12—The simulation of a crack appearance and propagation.

Table III. Comparison of the Results of Different Model Microstructures with B206 Alloy (As Cast)

Alloy/Model	Young's Modulus (GPa)	Yield Stress (MPa)	Ultimate Stress (MPa)	Elongation (pct)
B206 as cast <sup>[24]</sup>	≈72	160 to 172	232 to 255	2.8 to 5
Microstructure of Fig. 7(c)	72.23	165	236	2.3
Microstructure of Fig. 7(d)	71.39	167	245	2.4

Elimination of a small element from the mesh creates a hole, or a crack, inside the material. As a result, stress concentration will be formed around the crack which affects the neighboring elements. So the crack propagates inside the material until macroscopic failure. Using the generated microstructures, this phenomenon can be simulated easily. Figures 12(a) through (d) show how a single crack appears and propagates inside the RVE. These figures present the Von-mises stresses near a crack. They have been produced from the *general static* finite element analysis with ABAQUS.

## V. THE VARIABLES AFFECTING THE ELASTIC PROPERTY OF A MATERIAL

Having the above grain generation method and solving the finite element models with different grain shapes and grain generation parameters, it can be concluded that the following parameters affect the elastic characteristic of a solid material:

- Phase fractions: increasing a phase fraction increases or decreases the overall material properties. The phase fraction mainly depends on the cooling conditions and heat treatment procedure.
- Phase distribution over the domain: if phases distribute uniformly over the domain more uniform stress distribution over the domain is produced which affects the mechanical properties of the material.
- Grain shape and size: grain shape and size effect how adjacent grains contact to each other and the amount of  $\theta$  phase between the grains. As a result, it affects the stress distribution inside the control volume.

Besides the above parameters, this microstructure generation method has different other random parameters, so using the same basic grain shapes, for the same control volume, different microstructures can be created.

Although these generated microstructures have different shapes, because of these random parameters, the overall characteristics of the whole RVE are the same and the calculated material properties are varying inside a narrow interval which is comparable to the variation of experimental measured values using different test samples as reported in Reference 24.

## VI. CONCLUSIONS

Using a simple numerical procedure, the discretized microstructures have been generated to mimic a realistic multiphase grain microstructure. A predefined basic grains database was used and a complex grain microstructure can be constructed with these shapes. The time consuming grain growth procedures have not been used in this approach, which simplifies the method a lot. Zones of different phases can be formed between the generated grains. The presence of intergranular secondary phases is assumed. The grain structure inside a given RVE is automatically transformed into a finite element mesh. Using a commercial finite element code, the mechanical

properties of an as-cast binary aluminum 4.6 pct copper alloy was calculated. Our results match very well with the experimental results. The stress distribution inside the heterogeneous material model has been presented. The fracture phenomena, crack apparition, and propagation, in the as-cast material is also simulated.

Although, we have used this method for a binary aluminum alloy, it has the capacity to be used for the generation of other material microstructures. This model is also extendable to a 3D granular model.

## REFERENCES

1. R. Phillips: *Curr. Opin. Solid State Mater. Sci.*, 1998, vol. 3 (6), pp. 526–32.
2. D. Raabe: *Computational Materials Science: The Simulation of Materials Microstructures and Properties*, 1st ed., Wiley-VCH, New York, NY, 1998, p. 233.
3. K.W. Mahin, K. Hanson, and J.W. Morris, Jr.: *Acta Metall.*, 1980, vol. 28, pp. 443–53.
4. H.J. Frost, J. Whang, and C.V. Thompson: in *Proc. 7th RISØ International Symposium on Materials Science*, N. Hansen, D. Juul Jensen, T. Leffers, and B. Ralph, eds., RJSØ National Laboratory, Roskilde, 1986, p. 315.
5. F.J. Humphreys: *Acta Mater.*, 1997, vol. 45 (10), pp. 4231–40.
6. F.J. Humphreys: *Acta Mater.*, 1997, vol. 45 (12), pp. 5031–39.
7. D. Juul Jensen: *Scripta Metall. Mater.*, 1992, vol. 27, pp. 1551–56.
8. D. Juul Jensen: *Metall. Mater. Trans. A*, 1997, vol. 28A, pp. 15–25.
9. Y.Z. Wang and L.Q. Chen: *Simulation of Microstructure Evolution, Methods in Materials Research*, E.N. Kaufmann, R. Abbaschian, A. Bocarsly, et al., eds., Wiley, New York, NY, 1999.
10. L. Madej, L. Rauch, K. Perzynski, and P. Cybulka: *Arch. Civil Mech. Eng.*, 2011, vol. 11, pp. 661–79.
11. L. Madej, L. Sieradzki, M. Sitko, K. Perzynski, K. Radwanski, and R. Kuziak: *Comput. Mater. Sci.*, 2013, vol. 77, pp. 172–81.
12. M. Ortiz and R. Phillips: *Adv. Appl. Mech.*, 1998, vol. 36, pp. 1–79.
13. P.R. Dawson and E.B. Marin: *Adv. Appl. Mech.*, 1998, vol. 34, pp. 77–169.
14. A.J. Beaudoin, H. Mecking, and U.F. Kocks: *Philos. Mag. A*, 1996, vol. 73, pp. 1503–17.
15. R. Becker: *Acta Metall.*, 1991, vol. 39, pp. 1211–30.
16. P.E. McHugh, R.J. Asaro, and C.F. Shih: *Acta Metall.*, 1993, vol. 41, pp. 1461–76.
17. W. Kurz and D.J. Fischer: *Fundamentals of Solidification*, 3rd ed., Trans Tech, Dürnten, 1992, p. 118.
18. D. Larouche: *CALPHAD*, 2007, vol. 31, pp. 490–504.
19. B. Dutta, O. Pompe, and M. Rettenmayr: *Mater. Sci. Technol.*, 2004, vol. 20, pp. 1011–18.
20. J.E. Bresenham: *IBM Syst. J.*, 1965, vol. 4 (1), pp. 25–30.
21. G.C. Hasson and C. Goux: *Scripta Metall.*, 1971, vol. 5, pp. 889–94.
22. V. Mathier, A. Jacot, and M. Rappaz: *Model. Simul. Mater. Sci. Eng.*, 2004, vol. 12, pp. 479–90.
23. M. Rappaz, A. Jacot, and W.J. Boettinger: *Metall. Mater. Trans. A*, 2003, vol. 34A, pp. 467–79.
24. H.K. Kanga, D. Larouche, M. Bournane, and A. Rahem: *Int. J. Cast Met. Res.*, 2012, vol. 25 (1), pp. 15–25.
25. S. Vernède and M. Rappaz: *Acta Mater.*, 2007, vol. 55, pp. 1703–10.
26. F.R. Eshelman and J.F. Smith: *J. Appl. Phys.*, 1978, vol. 49, pp. 3283–88.
27. D. Levasseur and D. Larouche: *Mater. Sci. Eng. A*, 2011, vol. 528, pp. 4413–21.
28. M. Kutz: *Handbook of Materials Selection*, Wiley, New York, NY, 2002.
29. M. Tiryakioglu, J. Campbell, and N.D. Alexopoulos: *Mater. Sci. Eng. A*, 2009, vol. 506, pp. 23–26.
30. ABAQUS 6.12 Documentations, ABAQUS Analysis User's Manual, Section 24.2.2, Dassault Systèmes, 2012.
31. W.F. Smith: *Foundations of Materials Science and Engineering*, 2nd ed., McGraw-Hill, New York, NY, 1993.